DQ-Frame Impedance Measurement of Three-Phase Converters Using Time-Domain MIMO Parametric Identification

Hong Gong, *Student Member, IEEE*, Xiongfei Wang, *Senior Member, IEEE*, and Dongsheng Yang, *Senior Member, IEEE*

***Abstract*—The *dq*-frame impedance model is increasingly employed to analyze the grid-converter interactions in three-phase systems. As the impedance model is derived at a specific operating point, it is required to connect the converter to actual power grids during the impedance measurement. Yet, the nonzero grid impedance causes cross-couplings between perturbation and response signals, which consequently jeopardize the accuracy of impedance measurement. This article analyzes first the coupling effect of the grid impedance on the measured impedance, and then proposes a multiple-input multiple-output parametric impedance identification method for mitigating the effect. Instead of using the fast Fourier transform, the method allows for obtaining the parametric impedance model directly from the time-domain data. Further, with the simultaneous wideband excitations, only a single measurement cycle is needed. The effectiveness of the method is verified in both simulations and experimental tests.**

***Index Terms*—Coupling effect, impedance measurement, multiple-input multiple-output (MIMO) parametric identification small-signal model.**

I. Introduction

As converter-based resources are increasingly integrated into power grids, power-electronic-based power systems are being built in the near future [1]. The interactions between the multiple-timescale control dynamics of converters and the grid tend to cause oscillations in a wide frequency range [2]. To address the challenges, the impedance-based modeling and stability analysis methods have been extended to converter-based power systems [3]–[5]. Yet, the analytical impedance model is difficult for system operators to obtain since they usually have no access to the control systems of converters from different vendors. There is thus growing demand for measuring the "black-box" impedance model directly from the terminals of converters.

Manuscript received January 12, 2020; revised May 26, 2020; accepted July 3, 2020. Date of publication July 9, 2020; date of current version September 22, 2020. Recommended for publication by Associate Editor R. Burgos. *(Corresponding author: Xiongfei Wang.)*

Hong Gong and Xiongfei Wang are with the Department of Energy Technology, Aalborg University, 9220 Aalborg, Denmark (e-mail: hgo@et.aau.dk; xwa@et.aau.dk).

Dongsheng Yang is with the Department of Electrical Engineering, Electrical Energy Systems Group, Eindhoven University of Technology, Eindhoven 5612, The Netherlands (e-mail: d.yang1@tue.nl).

Color versions of one or more of the figures in this article are available online at https://ieeexplore.ieee.org.

Digital Object Identifier 10.1109/TPEL.2020.3007852

The impedance measurement techniques for dc–dc converters have been well developed [6], [7]. In contrast, for three-phase ac systems, the converter impedance is generally developed in the *dq*-frame, since the time-periodic ac operating trajectories are transformed into time-invariant dc operating (equilibrium) points. Consequently, the *dq*-frame impedance model of three-phase converters is an MIMO system, and thus the Generalized Nyquist Stability Criterion is used for the stability assessment of grid-converter interactions [8].

Continuous research efforts have been made for measuring the *dq*-fame impedance of three-phase converters. A general method is based on the linear superimposition principle, where either *d*- or *q*-axis is perturbed with small excitations, while the other axis is kept unchanged [9], [10], thus the entries of the impedance matrix can be obtained one by one. However, in the presence of the grid impedance, the cross-couplings between the *d*- and *q*-axis of the grid impedance matrix, i.e., the nondiagonal entries of the matrix are non zero, are inevitable. Consequently, when measuring the converter impedance, the perturbation injected at one axis will be coupled with the other axis through the cross-coupling terms of the grid impedance matrix [11], and hence, the accuracy of measuring the converter impedance is affected by the grid impedance.

To address such a coupling effect of the grid impedance, two linearly independent perturbations are sequentially injected into the system and then four equations can be obtained to calculate the impedance matrix [12], [13]. By identifying the decoupling matrix, which expresses the relationship between the uncoupled transfer functions and the identified coupled ones, the coupling effect of the grid impedance on the measured impedance results can be mitigated [14]–[16]. However, this approach requires multiple measurement cycles to sequentially identify the entries of the converter impedance matrix, which is time-consuming. Further, the versatile renewable energy sources tend to shift the operating points of converters, which can lead to inaccurate measurement results if the impedance measurement takes a long time.

To achieve an efficient impedance measurement, the MIMO identification technique is recently developed [17]–[20], where two uncorrelated excitation signals are simultaneously injected at the *d*- and *q*-axis. By setting different frequencies for the two perturbations, the diagonal entries of the converter impedance matrix can be calculated simultaneously, which greatly reduces

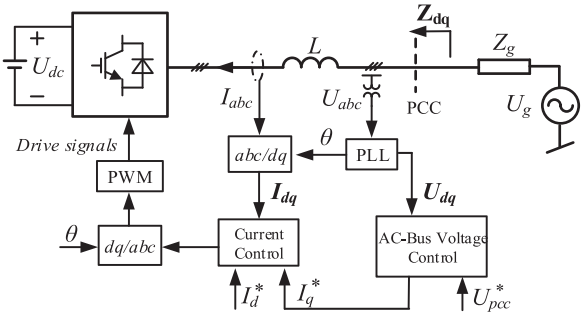

Fig. 1. Simplified one-line diagram of a three-phase grid-connected VSC.

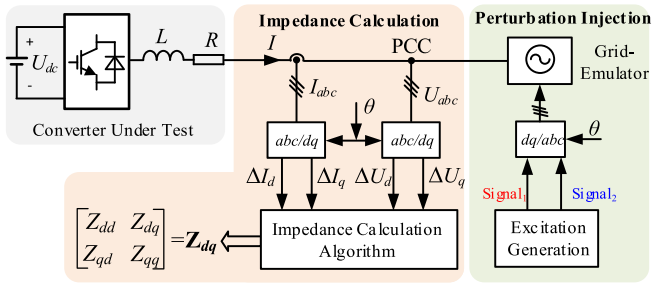

Fig. 2. System diagram of the conventional MIMO impedance measurement setup.

the impedance measurement time. Nevertheless, those works overlook the cross-coupling effect of the grid impedance, and thus the perturbation signals at the *d*- and *q*-axis, are correlated with each other, which can lead to inaccurate impedance calculations in the frequency-domain [9]–[11], [17]–[20]. Further, when the measured responses contain multiple frequency components, an appropriate time window is required for using the FFT, in order to avoid the spectrum leakage [20].

This article proposes a time-domain MIMO impedance identification technique to address the cross-coupling effect of the gird impedance and improve the efficiency of impedance measurement. In the approach, by minimizing the prediction error between the predicted model and actual model, the impedance calculation is merely based on uncorrelated excitation signals, which are not influenced by the grid impedance. Moreover, with the simultaneous injection of wideband excitation signals, the parametric impedance matrix is obtained directly from the time-domain data in a single measurement cycle. Thus, the use of FFT is avoided, and computational efficiency can be significantly enhanced. Simulations and experimental tests confirm the effectiveness of the method.

II. Impedance Measurement of Three-Phase Converters

A. System Description

Fig. 1 illustrates a simplified one-line diagram of a three-phase grid-connected voltage source converter (VSC), where L is the filter inductor and Z_g denotes the grid impedance, including grid capacitor C_g and inductor L_g. I_{abc} and U_{abc} are three-phase inductor currents and three-phase voltages at the point of common coupling (PCC), respectively. A constant dc-link voltage $U_{\rm dc}$ is assumed, while the ac-bus voltage control, the current control, and the phase-locked loop (PLL) are considered. θ denotes the phase angle measured by the PLL. Z_{dq} is the *dq*-frame impedance matrix of the converter, which characterizes the dynamic behavior at the PCC of the VSC.

The relationships between voltage perturbations and current responses at the *d*- and *q*-axis are used to model the *dq*–frame impedance characteristics of the VSC, which are given by

$$\begin{bmatrix} \Delta U_d \\ \Delta U_q \end{bmatrix} = \mathbf{Z}_{dq} \begin{bmatrix} \Delta I_d \\ \Delta I_q \end{bmatrix} = \begin{bmatrix} Z_{dd} & Z_{dq} \\ Z_{qd} & Z_{qq} \end{bmatrix} \begin{bmatrix} \Delta I_d \\ \Delta I_q \end{bmatrix} \quad (1)$$

where Δ denotes the small variations of voltage and current from the equilibrium points.

To measure the *dq*-frame impedance of the VSC, two uncorrelated perturbations are sequentially injected into the system and then four equations can be obtained to calculate the impedance matrix, as

$$\begin{bmatrix} Z_{dd} & Z_{dq} \\ Z_{qd} & Z_{qq} \end{bmatrix} = \begin{bmatrix} U_{d1}^m & U_{d2}^m \\ U_{q1}^m & U_{q2}^m \end{bmatrix} \begin{bmatrix} I_{d1}^m & I_{d2}^m \\ I_{q1}^m & I_{q2}^m \end{bmatrix}^{-1} \quad (2)$$

where the subscripts '1' and '2' imply two linearly independent perturbations. However, this impedance measurement method requires multiple measurement cycles to sequentially calculate the impedance entries, which is time-consuming [12]. To achieve the efficient impedance measurement, the MIMO impedance measurement method is thus proposed.

B. MIMO Impedance Measurement of Three-Phase Converters in the dq-Frame

Fig. 2 illustrates the diagram of the conventional MIMO impedance measurement setup, which is composed of the perturbation injection and the impedance calculation [17]–[20]. To measure the impedance of VSCs, small excitation signals are usually injected into the system, and then the resulted responses of PCC voltage and current are used to calculate the impedances [23].

A variety of signals can be used to excite the VSC system, which is generally selected based on the signal-to-noise ratio, the measurement time, and the immunity of nonlinear effect [11]. A sinusoidal signal is a basic form of excitation signals, which is implemented with either a single-frequency component [13] or multifrequency components at a time [24]. It is generally expected to save the measurement time by using the multifrequency sinusoidal signals. However, the sum of multiple sinusoidal signals may lead to a high magnitude of the excitation signal, whose accuracy is challenged by the inherent nonlinear effect of the VSC [24]. To overcome this limitation, another form of multi-frequency signal, i.e., the pseudorandom binary sequence (PRBS)signal, is used in this article for the fast measurement of converter impedance.

As shown in Fig. 2, the perturbation is injected through the grid emulator and there is no grid impedance connected with the VSC. To achieve the efficient measurement of the *dq*-frame impedance matrix of VSC, two uncorrelated excitation signals

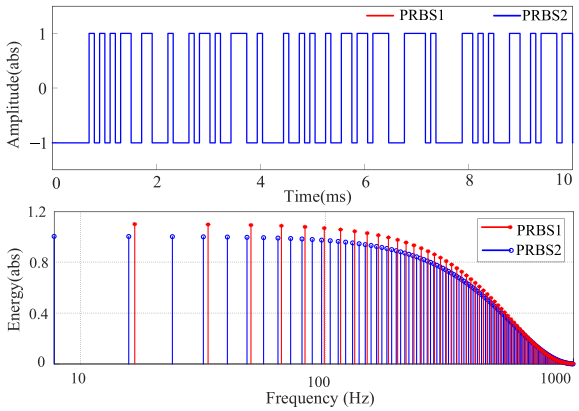

Fig. 3. Samples of two uncorrelated PRBSs in the time-domain and frequency-domain.

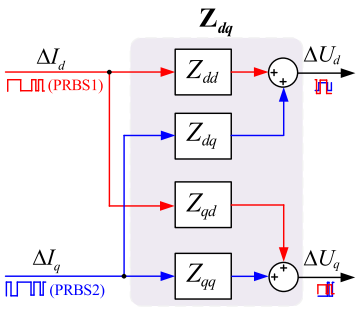

Fig. 4. Conventional MIMO impedance calculation without considering the grid impedance.

are required to simultaneously inject into the system [12]. Two PRBSs at different frequency points are designed as the uncorrelated excitation signals for fully exciting the MIMO system. The first PRBS is generated at 1020 Hz by a 7-bit-length shift register while the second PRBS is generated at 1000 Hz by a 6-bit-length shift register. Fig. 3 shows the samples of two uncorrelated PRBSs in the time-domain and frequency-domain. The energies are located in different frequencies between two PRBSs and the energies of both excitation signals drop to zero at the generation frequency.

Fig. 4 illustrates the conventional MIMO impedance calculation, where the grid impedance is not considered, and the actual perturbation signals applied for converters are uncorrelated with each other [13].

The excitation signal, PRBS1 is imposed on the *d*-axis while the PRBS2 is simultaneously imposed on the *q*-axis. Then, the responses of voltages ΔU_d and ΔU_q are not only from the contribution of PRBS1, but also from the contribution of PRBS2. By using the cross-correlation technique [17], the responses can be decomposed into ΔU_{dq1} and ΔU_{dq2} in the frequency-domain, where the subscripts "1" and "2 imply the response from the contribution of PRBS1 and PRBS2, respectively. Thus, the impedance Z_{dd}, Z_{qd} can be easily identified and expressed as

$$Z_{dd} = \frac{\Delta U_{d1}}{\Delta I_d}\Big|_{\Delta I_q=\text{PRBS2}} . \tag{3}$$

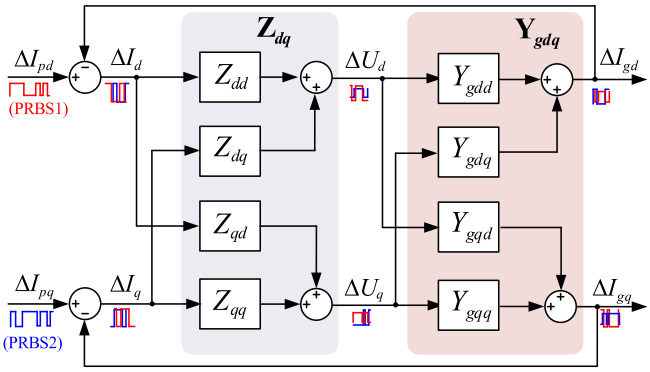

Fig. 5. Coupling influence of grid impedance on measured converter impedance with simultaneous injection of two uncorrelated PRBSs.

Similarly, the impedance Z_{dq}, Z_{qq} can then be simultaneously calculated as

$$Z_{dq} = \frac{\Delta U_{d2}}{\Delta I_q}\Big|_{\Delta I_d=\text{PRBS1}} . \tag{4}$$

According to the data of input and output of (3) and (4), the impedance transfer functions can be readily obtained by using parametric identification algorithms [25], [26]. It is noted that the MIMO impedance matrix of the converter is decomposed into four SISO systems when the uncorrelated excitation signals are perturbed on the *dq*-axis simultaneously.

III. Coupling Effect of Grid Impedance on Measured Converter Impedance

In the practical application, the excitation signals are not injected by the grid emulator and the converter is connected to actual power grids. The grid impedance may vary in a wide range in reality, and its effect on the conventional MIMO impedance measurement has to be considered. Fig. 5 illustrates the coupling effect of grid impedance on the measured converter impedance when two uncorrelated PRBSs are simultaneously injected into the system. It is clear that the perturbation signals ΔI_{dq} that are actually applied to converters differ from excitation signals ΔI_{pdq}, due to the additional feedback paths formed by the grid impedance [11]. Consequently, the cross-coupled perturbations are imposed on the VSC at the *d*- and *q*-axis, which makes the perturbation signals ΔI_d and ΔI_q used for the impedance calculation correlated with each other [12].

Given PRBS1 imposed on the *d*-axis and PRBS2 simultaneously imposed on the *q*-axis, the responses of the voltages ΔU_d and ΔU_q can be decomposed into ΔU_{dq1} and ΔU_{dq2} in the frequency-domain, respectively. ΔU_{dq1} are not only caused by ΔI_{d1} but ΔI_{q1} due to the existence of disturbance voltage ΔI_{gq1}, whose relationships can be derived as follows:

$$\frac{\Delta U_{d1}}{\Delta I_{d1}} = Z_{dd} + Z_{dq}\frac{\Delta I_{q1}}{\Delta I_{d1}}\Big|_{\Delta I_{q1}=-\Delta I_{gq1}} \tag{5}$$

$$\frac{\Delta U_{q1}}{\Delta I_{d1}} = Z_{qd} + Z_{qq}\frac{\Delta I_{q1}}{\Delta I_{d1}}\Big|_{\Delta I_{q1}=-\Delta I_{gq1}} \tag{6}$$

where ΔI_{q1} is due to the grid admittance and can be given by

$$\Delta I_{q1} = -\Delta I_{gq1} = -Y_{gqd}\Delta U_{d1} - Y_{gqq}\Delta U_{q1}. \quad (7)$$

Substituting (7) into (5) and (6), respectively, the resulting impedance entries associated with the *d*-axis excitation (PRBS1) can be obtained as

$$\frac{\Delta U_{d1}}{\Delta I_{d1}} = \frac{Z_{dd} + Y_{gqq}Z_{qq}Z_{dd} - Z_{qd}Z_{dq}Y_{gqq}}{1 + Y_{gqq}Z_{qq} + Y_{gqd}Z_{dq}} \neq Z_{dd} \quad (8)$$

$$\frac{\Delta U_{q1}}{\Delta I_{d1}} = \frac{Z_{qd} + Y_{gqd}Z_{dq}Z_{qd} - Z_{dd}Z_{qq}Y_{gqd}}{1 + Y_{gqq}Z_{qq} + Y_{gqd}Z_{dq}} \neq Z_{qd}. \quad (9)$$

Considering the responses from the contribution of PRBS2, the corresponding impedance entries Z_{dq} and Z_{qq} can be simultaneously calculated by

$$\frac{\Delta U_{d2}}{\Delta I_{q2}} = Z_{dq} + Z_{dd}\frac{\Delta I_{d2}}{\Delta I_{q2}}\Big|_{\Delta I_{d2}=-\Delta I_{gd2}} \quad (10)$$

$$\frac{\Delta U_{q2}}{\Delta I_{q2}} = Z_{qq} + Z_{qd}\frac{\Delta I_{d2}}{\Delta I_{q2}}\Big|_{\Delta I_{d2}=-\Delta I_{gd2}}. \quad (11)$$

Due to the influence of the grid admittance, the *d*-axis disturbance current can also be derived as

$$\Delta I_{d2} = -\Delta I_{gd2} = -Y_{gdd}\Delta U_{d2} - Y_{gdq}\Delta U_{q2}. \quad (12)$$

Consequently, the resulting impedance entries associated with the *q*-axis excitation (PRBS2) can be obtained as follows, which are also dependent on the grid admittance:

$$\frac{\Delta U_{d2}}{\Delta I_{q2}} = \frac{Z_{dq} + Y_{gdq}Z_{qd}Z_{dq} - Z_{qq}Z_{dd}Y_{gdq}}{1 + Y_{gdq}Z_{qd} + Y_{gdd}Z_{dq}} \neq Z_{dq} \quad (13)$$

$$\frac{\Delta U_{q2}}{\Delta I_{q2}} = \frac{Z_{qq} + Y_{gdd}Z_{dd}Z_{qq} - Z_{dq}Z_{qd}Y_{gdd}}{1 + Y_{gdq}Z_{qd} + Y_{gdd}Z_{dq}} \neq Z_{qq}. \quad (14)$$

It is clear that the calculated impedance entries are dependent on the grid admittance. When the grid admittance is small, the converter admittance model can be approximately equal to (3) and (4). However, when the grid impedance is nonnegligible, the cross-coupling perturbations between the *d*- and *q* axis have to be considered in the converter impedance measurement. Therefore, during the MIMO impedance measurement, the VSC cannot be simply treated as four SISO systems, but a MIMO system.

IV. Time-Domain MIMO Parametric Identification

To obtain an accurate impedance of the VSC with a nonzero grid impedance/admittance, the time-domain MIMO parametric impedance identification technique based on the prediction error method (PEM) is introduced in this section. The step-by-step implementation of the approach will be discussed in Section V.

Fig. 6 illustrates the block diagram of the time-domain MIMO parametric impedance identification approach, where the basic idea is to find the appropriate transfer functions of the identified impedance model Z_{dq}^{ϕ} based on the time-domain responses so that the identified model can accurately describe the actual impedance model Z_{dq}^{0}. It is noted that the transfer function is identified in the discrete domain based on discrete data, which can be converted to the continuous domain if necessary.

In the approach, to fully excite the MIMO system and guarantee the accuracy of the identification, two uncorrelated excitation

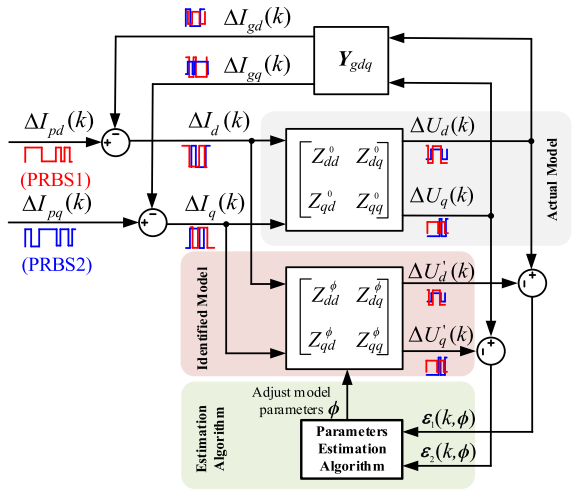

Fig. 6. Block diagram of the time-domain MIMO impedance identification approach.

signals $\Delta I_{pd}(k)$ (PRBS1) and $\Delta I_{pq}(k)$ (PRBS2) are simultaneously injected into the system [27], and the responses of $\Delta I_d(k)$, $\Delta I_q(k)$, $\Delta U_d(k)$ and $\Delta U_q(k)$ are measured to identify the impedance model in the time-domain, where *k* denotes the *k*th sampling point. The structure and order of the identified model are first selected. The PEM is then used to establish the relationship between the estimated parameters of the transfer functions and the measured response. Next, the least-squares method is implemented to obtain the sum of squared prediction errors (i.e., the cost function) between the outputs from the identified model and actual outputs. The cost function is finally optimized by using the gradient descent algorithm [27] and the parameters of the identified impedance model will be adjusted constantly until the prediction error approaches to zero, which makes the identified impedance Z_{dq}^{ϕ} approximately equal to the actual impedance model Z_{dq}^{0}.

A. Identified Model Structure and Order

The selection of the appropriate structure of the general transfer function model plays an important role in the identification of the MIMO system, as it determines the number of parameters, the convergence, and the computational effort [28]. Depending on whether the transfer functions have a common denominator, the model structure can be classified into equation-error model (EEM) and output-error model [29]. To reduce the number of identified parameters and facilitate the selection of model order, one of the simplified EEMs, e.g., AutoRegressive with eXogenous input (ARX) [25], can be obtained as shown in (15). According to Fig. 6, one of the predicted outputs $\Delta U_d'(k)$ is taken as an example for elaborating the identification process.

Supposing that the predicted data has been generated by (where the noise model is excluded for brevity)

$$\Delta U'_d(k) = \frac{B_{11}(z)}{A_1(z)}\Delta I_d(k) + \frac{B_{12}(z)}{A_1(z)}\Delta I_q(k)$$
$$= Z_{dd}^{\phi}(z)\Delta I_d(k) + Z_{dq}^{\phi}(z)\Delta I_q(k) \quad (15)$$

where $Z_{dd}^{\phi}(z)$ and $Z_{dq}^{\phi}(z)$ represent the identified transfer functions of the impedance model for VSC. The operator z is a shift operator meaning $z^{-1}\Delta U_d'(k) = \Delta U_d'(k-1)$ and it will be omitted in the following whenever appropriate. $A_1(z)$, $B_{11}(z)$ and $B_{12}(z)$ are the polynomials of the transfer functions, which can be written as

$$\begin{cases} A_1(z) = a_{10} + a_{11}z^{-1} + \ldots. + a_{1m}z^{-m} \\ B_{11}(z) = b_{110} + b_{111}z^{-1} + \ldots. + b_{11n}z^{-n} \\ B_{12}(z) = b_{120} + b_{121}z^{-1} + \ldots. + b_{12p}z^{-p}. \end{cases} \tag{16}$$

The parameters vector of transfer functions is defined as

$$\phi = (a_{10} \ldots . a_{1\boldsymbol{m}} \,|b_{110} \ldots b_{11\boldsymbol{n}} \,|b_{120} \ldots b_{12p}) \tag{17}$$

where *m*, *n,* and *p* mean the order of the polynomials. Thus, the purpose of the identification is to estimate the parameters given in (17), such that the identified model can accurately describe the actual model.

The order of $A_1(z)$, $B_{11}(z)$ and $B_{12}(z)$ determine the number of coefficients of each polynomial. If we increase the order, it will increase the computational complexity while if we reduce the order, the accuracy of the estimated model will be compromised. There is a tradeoff between the computational complexity and accuracy of the identified impedance model. Singular value decomposition (SVD) is usually used to estimate the order of the identified model [28]. If the noise is not taken into account, the order estimation of the identified system is easy. The number of nonzero singular values is equal to the order of the system. However, when considering the influence of the noise, the data matrix will be of the full rank and all singular values σ_i are nonzero. The rank of the identified system has to be chosen from the number of significant singular values. The ratio between singular values can be considered as the determination of the identified model order, which can be expressed by

$$\frac{\sigma_n}{\sigma_{n+1}} = \max\left\{\frac{\sigma_1}{\sigma_2}, \frac{\sigma_2}{\sigma_3}, \ldots.., \frac{\sigma_i}{\sigma_{i+1}}\right\} \tag{18}$$

where *n* is the estimated order of the identified model.

Based on SVD of the data matrix for measured responses, the highest order of the identified model can be chosen as the initial order of each polynomial [29], and the final selection of the model order is done by iteratively checking the fitting accuracy.

B. Parameters Estimation Algorithm

The PEM is used to build the relationship between the parameters of the identified model and the actual response of the plant. The prediction error between the actual output $\Delta U_d(k)$ and the predicted output $\Delta U_d'(k)$ from the identified model can be written as

$$\begin{aligned} \varepsilon_1(k,\phi) &= \Delta U_d(k) - \Delta U'_d(k) \\ &= (Z_{dd}^0 - Z_{dd}^{\phi})\Delta I_d(k) + (Z_{dq}^0 - Z_{dq}^{\phi})\Delta I_q(k) \end{aligned} \tag{19}$$

where $Z_{dd}^0(z)$ and $Z_{dq}^0(z)$ are the actual discrete transfer functions of the impedance matrix entries.

When considering the coupling effect of the grid admittance, the input signals $\Delta I_d(k)/\Delta I_q(k)$ used for the impedance calculation are correlated with each other, and consequently, their effects on the specific responses cannot be distinguished. However, when using the PEM, as shown in (19), $Z_{dd}^0 - Z_{dd}^{\phi}$ and $Z_{dq}^0 - Z_{dq}^{\phi}$ should be always approximately equal to zero to guarantee the prediction error to be zero. This is because the input signals, ΔI_d and ΔI_q, are composed of two uncorrelated signals and cannot get the minimum value of the function (19) unless the identified model is equal to the actual model. Thus, the correlation of input signals caused by the coupling effect of grid impedance does not jeopardize the accuracy of the impedance measurement when using the PEM.

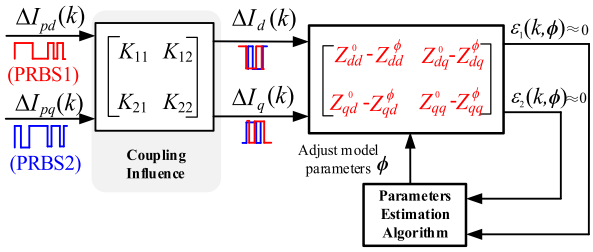

Fig. 7. Equivalent MIMO parametric identification block considering the grid impedance effects.

Fig. 7 shows the block diagram of the equivalent MIMO parametric identification, considering the grid impedance. To prove that the PEM is not influenced by the correlation of the input signals caused by the coupling effect, the input signals $\Delta I_{dq}(k)$ used for the impedance calculation can be expressed as a function of uncorrelated excitation signals $\Delta I_{pdq}(k)$, which is given as follows:

$$\begin{bmatrix} \Delta I_d(k) \\ \Delta I_q(k) \end{bmatrix} = \underbrace{\begin{bmatrix} K_{11}(z) & K_{12}(z) \\ K_{21}(z) & K_{22}(z) \end{bmatrix}}_{\mathbf{K}} \begin{bmatrix} \Delta I_{pd}(k) \\ \Delta I_{pq}(k) \end{bmatrix} \tag{20}$$

where the input sensitivity function *K* is $K = (I + Z_{dq}Y_{gdq})^{-1}$.

Based on (19) and (20), the prediction error can be rewritten as

$$\begin{aligned} \varepsilon_1(k,\phi) = {} & [(Z_{dd}^0 - Z_{dd}^{\phi})K_{11} + (Z_{dq}^0 - Z_{dq}^{\phi})K_{21}]\Delta I_{pd}(k) \\ & + [(Z_{dd}^0 - Z_{dd}^{\phi})K_{12} + (Z_{dq}^0 - Z_{dq}^{\phi})K_{22}]\Delta I_{pq}(k). \end{aligned} \tag{21}$$

Once the model structure and order have been defined and a set of input-output data of length *N* has been collected, the estimation of the model parameters ϕ can then be obtained by minimizing the sum of the squared prediction errors, which is known as the least-squares method [28], i.e.,

$$\phi^* = \arg\min_{\phi} \frac{1}{N}\sum_{k=1}^{N}[\varepsilon_1(k,\phi)]^2 \tag{22}$$

where "arg min" denotes the minimum value of the function.

The excitation signals $\Delta I_{pd}(k)/\Delta I_{pq}(k)$, which are simultaneously injected into the system, are designed to be uncorrelated with each other. On the basis of this and Parseval's relation in [28] and [29], the following result is given:

$$\begin{aligned}\phi^* = \underset{\phi}{\operatorname{argmin}} \Bigg[& \int_{-\pi}^{\pi} \left| (Z_{dd}^0 - Z_{dd}^{\phi}) K_{11} + (Z_{dq}^0 - Z_{dq}^{\phi}) K_{21} \right|^2 \\ & \times \Phi_{I_{pd}}(\omega) d\omega \\ & + \int_{-\pi}^{\pi} \left| (Z_{dd}^0 - Z_{dd}^{\phi}) K_{12} + (Z_{dq}^0 - Z_{dq}^{\phi}) K_{22} \right|^2 \\ & \times \Phi_{I_{pq}}(\omega) d\omega \Bigg] \end{aligned} \tag{23}$$

where $\Phi_{Ipd}(\omega)$ and $\Phi_{Ipq}(\omega)$ mean the spectra of the uncorrelated excitation signals, and $\Phi_{Ipd}(\omega)$, $\Phi_{Ipq}(\omega) > 0$ for any ω. Thus, the following equations need to be satisfied to obtain the minimum value of the function (23) and make the prediction error approximately equal to zero

$$\begin{cases} \underbrace{(Z_{dd}^0 - Z_{dd}^{\phi})}_{X_1} K_{11} + \underbrace{(Z_{dq}^0 - Z_{dq}^{\phi})}_{X_2} K_{21} \approx 0 \\ \underbrace{(Z_{dd}^0 - Z_{dd}^{\phi})}_{X_1} K_{12} + \underbrace{(Z_{dq}^0 - Z_{dq}^{\phi})}_{X_2} K_{22} \approx 0 \end{cases} \tag{24}$$

which can be considered as linear equations with two variables, where X_1 and X_2 represent $Z_{dd}^0 - Z_{dd}^{\phi}$ and $Z_{dq}^0 - Z_{\mathrm{dq}}^{\phi}$, respectively. Since the determinant of the coefficient matrix K is not equal to zero (due to the measured system is stable), the solution of the equation (X_1, X_2) should be equal to zero. This means that as long as the simultaneously injected excitation signals are uncorrelated, and the determinant of the matrix K is nonzero, the PEM will assure that the identified transfer function matrix in the model set is closest to the actual one.

The gradient descent method [28] is finally used to find the minimum value of (19) and to estimate the corresponding parameters of transfer functions. The gradient of the prediction error with respect to the identified parameters (i.e., the sensitivity of these errors to parameters variations) $\psi(k, \phi)$ can be obtained as

$$\psi(k, \phi) \triangleq -\frac{\partial Z_{dd}^{\phi}}{\partial \phi} \Delta I_d(k) - \frac{\partial Z_{dq}^{\phi}}{\partial \phi} \Delta I_q(k). \tag{25}$$

Fig. 8 shows the principle of the gradient descent algorithm used for finding the minimum of a function. The fastest descent way is to take steps proportional to the opposite direction of the function's gradient at any given point (e.g., the initial condition). This is because the gradient points to the steepest direction of the function's generated surface at the given point. Thus, based on (25), the estimated parameters can be adjusted continuously in the direction of the negative gradient of $\psi(k, \phi)$ to achieve the minimum of (19), and meanwhile, obtain the parameters of the identified transfer functions.

V. Implementation of MIMO Parametric Impedance Identification Technique

Fig. 9 shows the flowchart for the implementation of the MIMO parametric identification technique based on PEM for the impedance measurement of VSC. It includes the excitation injection, signal preprocessing, and time-domain MIMO parametric identification and model validation, which is next explained in detail. There are commercial tools available to apply them in an easy way, such as the System Identification Toolbox of MATLAB [28], which is used in this article.

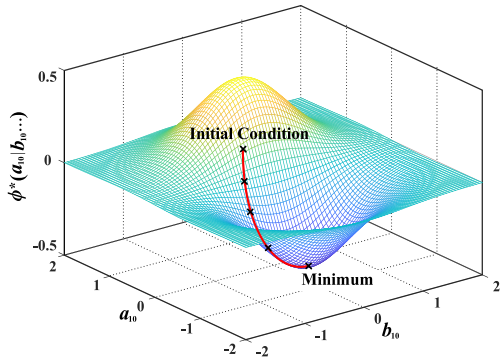

Fig. 8. Principle of the gradient descent algorithm.

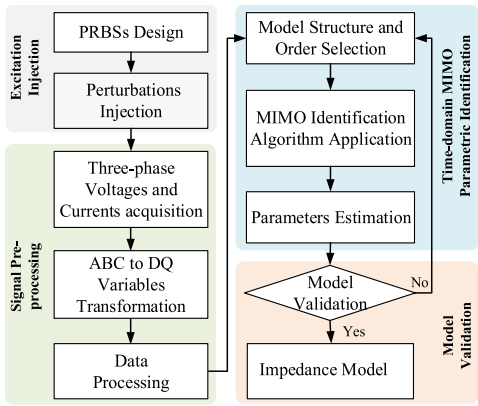

Fig. 9. Flowchart of MIMO identification for VSC impedance measurement.

A. Excitation Injection

For the excitation signal, PRBS should be carefully designed. The magnitude of PRBS plays an important role in the accuracy of the impedance measurement. On the one hand, the magnitude of the excitation signal has to be small to ensure that the system stays around its operating point. On the other hand, it has to be sufficiently large to reject noise disturbances. In general, the magnitude of the excitation signal is chosen between 5% and 10% of steady-state values [10], [11].

Two uncorrelated PRBSs, as shown in Fig. 3 are selected and designed, which are used for fully exciting the MIMO system. Next, the designed excitation signals are injected into the system by using either the existed converters or the established impedance measurement unit [13] to generate the response of voltage and current for VSC.

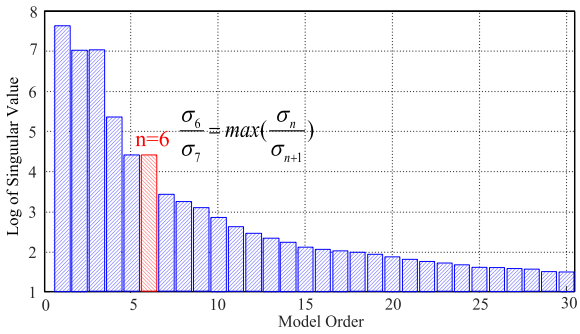

Fig. 10. SVD based on simulation data.

B. Signal Preprocessing

The response of voltage and current are first measured and recorded in *abc*-frame. To accurately and efficiently identify the impedance model of VSC, the measured input and output data must be further processed.

1) *dq-transformation:* First, the measured output current and voltage of VSC in the *abc*-frame are transformed into the *dq*-frame. It is noted that the influence of the synchronization phase angle has to be considered during the impedance calculation [30]. The low bandwidth of PLL used for the *dq*-transformation of the measured data is used in this article.
2) *Offset removal:* Second, the measured voltage and current have to subtract its mean values before the identification starts since the model identification is based on the small-signal perturbations of the measured signals.
3) *Measurement prefilter:* Finally, the filter can be used to prefilter both the measured voltage and current, which can focus the measured data on the frequency of the interest. Moreover, in order to lower the influence of the noise, several groups of input and output data can be obtained and averaged [19], which could be applied to identify the impedance model of VSC more accurately.

C. Time-Domain MIMO Parametric Identification

Next, the System Identification Toolbox can be used to do the time-domain MIMO parametric identification based on the processed voltages and currents. ARX is first chosen as the structure of the identified model in the toolbox. SVD is then implemented to obtain the singular values, which is used to determine the initial order of the identified model for the impedance identification.

Fig. 10 shows the SVD values according to the simulation data. The ratio between sequential singular values achieves the maximum when the identified model is equal to six. In practice, the order of the impedance model is usually selected to be higher than the number of dominant singular values to obtain satisfied performance due to the existence of noise in practical system identification.

The PEM is then used to get the relationship between the identified parameters and the measured data. The least-squares method is adopted to obtain the cost function of the prediction error and the gradient algorithm is selected to calculate the minimum value of the cost function and estimate parameters of the identified impedance matrix. The identified model is finally validated, which will be discussed in Section VI.

TABLE I
PARAMETERS OF THE VSC UNDER TEST

Symbol	Description	Value
K_{ac_p}/K_{ac_i}	Voltage outer controller	0.1/10
K_{i_p}/K_{i_i}	Current inner controller	7.85/274
K_p/K_i	PI controller of PLL	0.12/0.44
U_{acref}	AC voltage reference	200 V
ω	Grid frequency	314 rad/s
f_s	Sampling frequency	10 kHz
I_{d0}	*d* channel current steady value	8 A
I_{q0}	*q* channel current steady value	3.6 A
U_{d0}	*d* channel voltage steady value	200 V
U_{q0}	*q* channel voltage steady value	0 V
U_{dc0}	DC voltage of the converter	730 V
U_g	Grid phase-ground peak voltage	220 V
T_d	Dead-time	2 μs
L	Filtered inductor	3 mH
C_g	Grid capacitor	20 μF
L_g	Grid inductor	17 mH

VI. SIMULATION AND EXPERIMENT VERIFICATION

Since the admittance model of VSC is as the function of frequency, the verification of the identified admittance model can be carried out by comparing the analytical admittance model of VSC with the identified admittance model in the frequency domain. Further, a good model should be able to reproduce related data that have not been included in the identification process.

In this article, the identified model can be cross-validated by checking the response of the measured transfer functions of the admittance model against the measured response under the same input in the time domain. The fitting ratio (FR) defined in (26) is used to assess the fitting results between the two different sets of data

$$\mathrm{FR} = \left(1 - \frac{\sum_{k=0}^{N} [\boldsymbol{y}(k) - \hat{\boldsymbol{y}}(k)]^2}{\sum_{k=0}^{N} [\boldsymbol{y}(k)]^2}\right) \times 100\% \qquad (26)$$

where $y(k)$ and $\hat{\boldsymbol{y}}(k)$ are the data from the actual response of the system and the estimated admittance model, respectively; k represents sampling time; and N is the total sampled number for the validation. It is noted that the model structure or the model order needs to be selected again until the accuracy of the identified model satisfies the requirements.

Table I gives the parameters of the converter under test. To see the coupling influence of the grid impedance on impedance calculation, the ac voltage controller is adopted for the generation of the reactive current reference. In addition, a large grid impedance is also selected.

Table II gives the parameters of the converter that is considered as the excitation source to inject perturbation into the

TABLE II
PARAMETERS OF EXCITATION SOURCE

Symbol	Description	Value
K_{i_p1}/K_{i_i1}	Current inner controller	15/5480
K_{p1}/K_{i1}	PI controller of PLL	0.28/8.97
f_{s1}	Sampling frequency	10 kHz
I_{d01}	d channel current steady value	0 A
I_{q01}	q channel current steady value	0 A
U_{d01}	d channel voltage steady value	200 V
U_{q01}	q channel voltage steady value	0 V
U_{dc01}	DC voltage of the converter	730 V
T_{d1}	Dead-time	2 μs
L_1	Filtered inductor	3 mH

system, where the excitation signals are imposed on the dq-axis current references.

A. Simulation Verification

To verify the accuracy of the identified admittance model obtained through the proposed MIMO parametric identification algorithm, an impedance measurement setup is simulated.

According to the simulation data, the transfer functions of the identified admittance model are given. Based on the SVD, the lowest order that provides a good fit has been selected. Moreover, for simplicity, the model order reduction technique [27] is implemented. Therefore, the analytical expression of the identified admittance model can be found at the bottom of this page (z-domain, the sampling frequency is equal to 10 kHz)

Therefore, the comparison of frequency response for the admittance models is depicted, which are calculated from the theoretical model and the identified model, respectively, as shown in Figs. 11–14. All the admittance models are measured from 1 to 1000 Hz. It is noted that in a wide frequency range, the admittances Y_{dd}, Y_{qq}, Y_{dq}, and Y_{qd} identified through the proposed approach match well with the ones obtained through the theoretical calculation.

Furthermore, the accuracy of the identified model has been validated in the time-domain. Given the same excitation, the output currents in the simulation model and in the identified model are compared in Figs. 15 and 16. The two output currents of the identified model match the simulation output well (FR is equal to 92.87% and 92.5%, respectively), which means that the identified admittance model has the same output response as the simulation model in the time domain. Thus, the effectiveness of

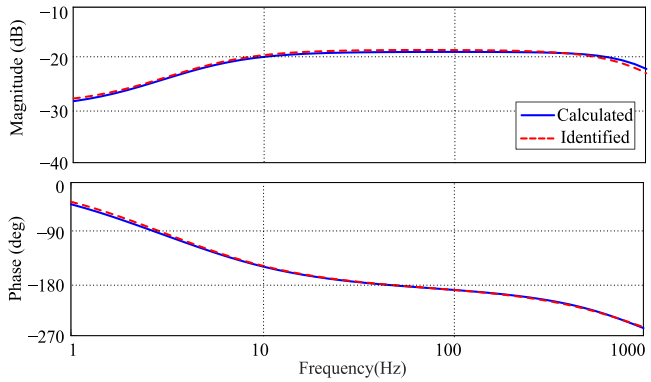

Fig. 11. Theoretically calculated admittance and identified admittance of Y_{dd}.

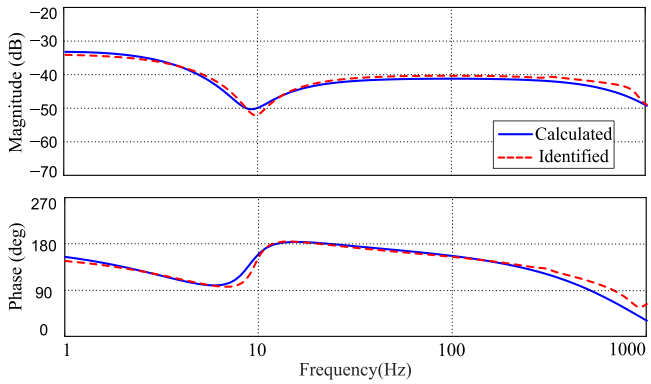

Fig. 12. Theoretically calculated admittance and identified admittance of Y_{dq}.

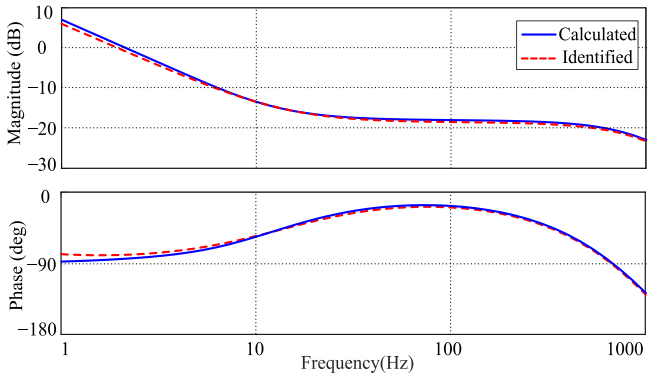

Fig. 13. Theoretically calculated admittance and identified admittance of Y_{qd}.

$$Y_{dd} = \frac{0.0004 - 0.082z^{-1} + 0.059z^{-2} - 0.02z^{-3} + 0.043z^{-4}}{1 - 0.2z^{-1} - 1.06z^{-2} + 0.03z^{-3} + 0.23z^{-4}}$$

$$Y_{dq} = \frac{0.0002 - 0.003z^{-1} + 0.005z^{-2} - 0.01z^{-3} + 0.018z^{-4} - 0.009z^{-5}}{1 - 1.07z^{-1} - 1.13z^{-2} + 1.11z^{-3} + 0.45z^{-4} - 0.36z^{-5}}$$

$$Y_{qd} = \frac{-0.0045 + 0.0039z^{-1} + 0.038z^{-2} + 0.033z^{-3} - 0.069z^{-4}}{1 - 0.52z^{-1} - 0.83z^{-2} + 0.40z^{-3} - 0.054z^{-4}}$$

$$Y_{qq} = \frac{-0.07z^{-1} + 0.1z^{-2} - 0.1z^{-3} + 0.13z^{-4} - 0.06z^{-5} + 0.03z^{-6}}{1 - 1.4z^{-1} + 0.54z^{-2} - 0.3z^{-3} - 0.5z^{-4} + 0.7z^{-5} + 0.2z^{-6}}$$

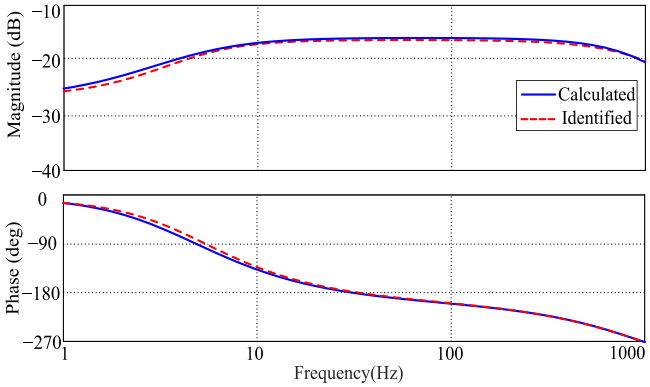

Fig. 14. Theoretically calculated admittance and identified admittance of Y_{qq}.

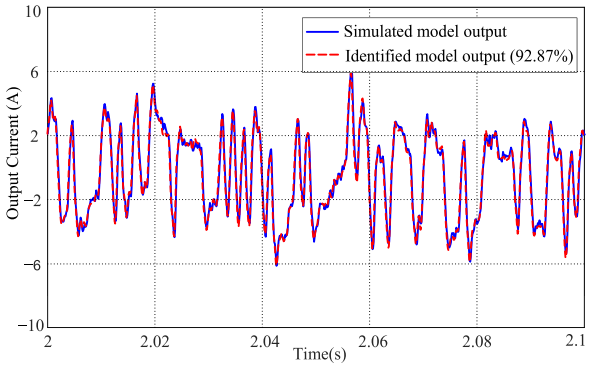

Fig. 15. *d*-axis current outputs of simulation and identified model under the same excitation input.

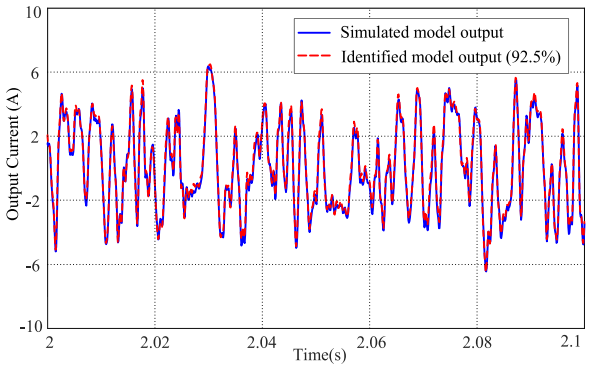

Fig. 16. *q*-axis current outputs of simulation and identified model under the same excitation input.

the proposed MIMO parametric impedance identification technique based on PEM is validated both in the frequency-domain and time-domain.

B. Experiment Verification

In order to further verify the correctness of the proposed method, a down-scale prototype based on the proposed impedance measurements setup, as shown in Fig. 3, is built.

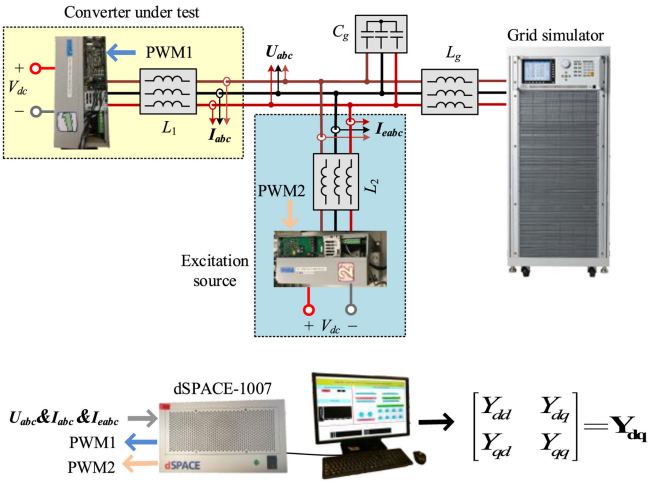

Fig. 17. Down-scale prototype of the impedance measurement.

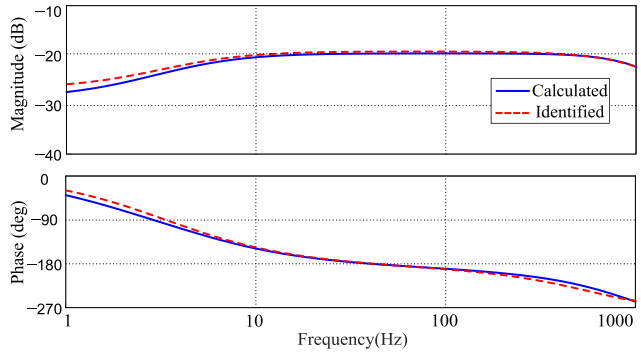

Fig. 18. Theoretically calculated admittance and identified admittance of Y_{dd}.

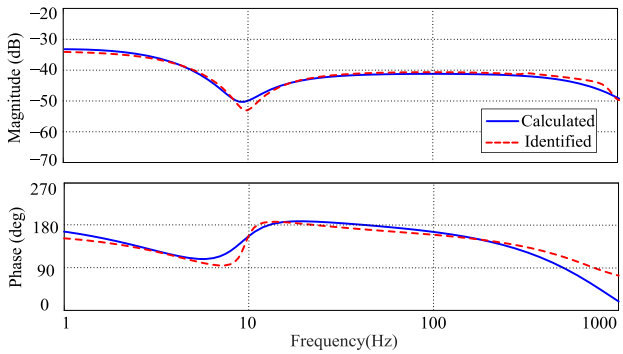

Fig. 19. Theoretically calculated admittance and identified admittance of Y_{dq}.

Yet, the shunt current injection is adopted because this method is much easier to implement for the experimental verification.

Fig. 17 shows the detailed experimental setup of the built impedance measurement unit. A programmable three-phase voltage source is used to emulate the power gird. Two VSCs are used, where one VSC is considered as the converter under test, and the other is used to inject perturbations. The current transducer LA55-P and the voltage transducer LV25-P are used

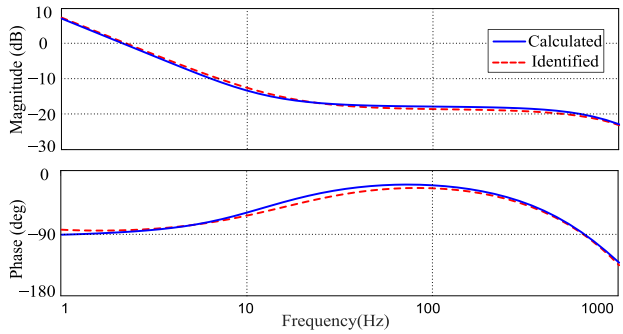

Fig. 20. Theoretically calculated admittance and identified admittance of Y_{qd}.

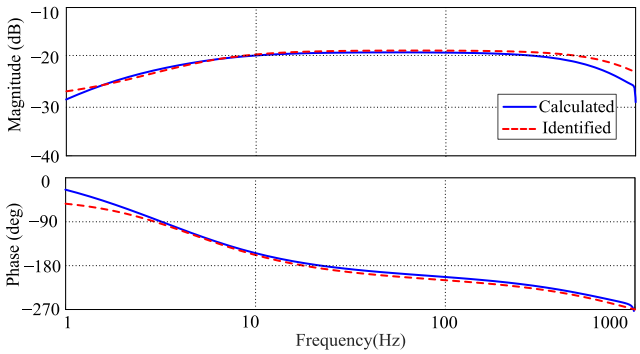

Fig. 21. Theoretically calculated admittance and identified admittance of Y_{qq}.

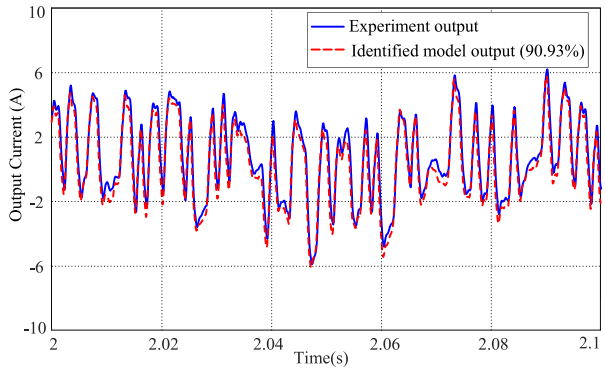

Fig. 22. d-axis current outputs of experiment and identified model under the same excitation input.

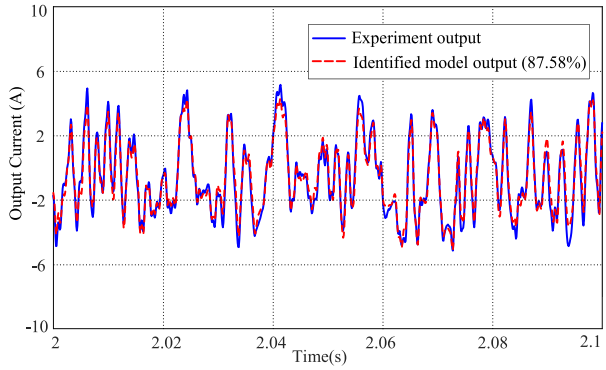

Fig. 23. q-axis current outputs of experiment and identified model under the same excitation input.

to acquire currents and voltages for the calculation of the admittance model. The sampling voltage and current are sent to the dSPACE and the synchronization phase was calculated based on the PLL and the voltage and current were recorded in the dq-domain.

In this system, the data is processed in the host computer and the admittance model is identified through the proposed MIMO parametric identification algorithm.

Similarly, according to the experiment data, the parametric expressions of the identified admittance model are given. Based on the SVD, the lowest order that provides a good fit has been selected, and the analytical expression of the identified admittance model is obtained as follows.

Furthermore, the frequency response of the theoretically calculated admittance and identified admittance based on the experiment data are shown in Figs. 18–21. It is clear that the admittance model of VSC identified from the experiment data matches well with the theoretically calculated admittance.

The accuracy of the identified model is also verified in the time domain through the recorded experiment data. Two output currents are compared under the same excitation input, as shown in Figs. 22 and 23. The comparison results show that the admittance model identified from the experiment data still match the theoretical impedance model well (FR is equal to 90.93% and 87.58%, respectively), which has the same conclusion as the simulation results and validates the correctness of the proposed MIMO parametric identification method for mitigating the coupling influence of the grid impedance.

$$Y_{dd} = \frac{0.006 - 0.065z^{-1} - 0.07z^{-2} + 0.07z^{-3} + 0.065z^{-4} - 0.005z^{-5}}{1 + 1.1z^{-1} - 1.4z^{-2} - 1.6z^{-3} + 0.4z^{-4} + 0.5z^{-5}}$$

$$Y_{dq} = \frac{-0.008z^{-1} + 0.006z^{-2} - 0.004z^{-3} + 0.004z^{-4} + 0.009z^{-5}}{1 - 0.71z^{-1} - 1.29z^{-2} + 0.23z^{-3} + 0.81z^{-4} + 0.41z^{-5}}$$

$$Y_{qd} = \frac{0.002 - 0.008z^{-1} + 0.026z^{-2} + 0.008z^{-3} - 0.028z^{-4}}{1 - 0.84z^{-1} - 0.84z^{-2} + 0.84z^{-3} - 0.16z^{-4}}$$

$$Y_{qq} = \frac{0.0005 + 0.073z^{-1} + 0.19z^{-2} - 0.21z^{-3} + 0.13z^{-4} - 0.04z^{-5}}{1 - 2.08z^{-1} + 1.08z^{-2} - 0.09z^{-3} + 0.26z^{-4} - 0.17z^{-5}}$$

VII. Conclusion

This article has revealed the coupling mechanism of the grid impedance, which leads to errors in the measured VSC impedance results if the conventional MIMO identification method is used. To mitigate the coupling influence and achieve the efficient impedance measurement, a time-domain MIMO parametric impedance identification technique based on PEM has been introduced. Compared with the conventional MIMO identification technique, the method employs the simultaneous wideband excitations to obtain the parametric impedance matrix of the VSC with a single measurement experiment, and the impedance model is directly identified from the time-domain data without using FFT, which saves the measurement time and ensures that the operating points of the system remain constant during the measurement. Moreover, the accuracy of the impedance measurement results is improved due to the mitigation of the coupling influence on impedance calculation caused by the grid impedance.

References

[1] B. Kroposki, B. Johnson, and Y. Zhang, "Achieving a 100% renewable grid: Operating electric power systems with extremely high levels of variable renewable energy," *IEEE Power Energy Mag.*, vol. 15, no. 2, pp. 61–73, Mar./Apr. 2017.

[2] X. Wang and F. Blaabjerg, "Harmonic stability in power electronic based power systems: Concept, modeling, and analysis," *IEEE Trans. Smart Grid*, vol. 10, no. 3, pp. 2858–2870, May 2019.

[3] X. Wang, F. Blaabjerg, and W. Wu, "Modeling and analysis of harmonic stability in an AC power-electronics-based power system," *IEEE Trans. Power Electron.*, vol. 29, no. 12, pp. 6421–6432, Dec. 2014.

[4] L. Harnefors, M. Bongiorno, and S. Lundberg, "Input-admittance calculation and shaping for controlled voltage-source converters," *IEEE Trans. Ind. Electron.*, vol. 54, no. 6, pp. 3323–3334, Dec. 2007.

[5] B. Wen, D. Dong, D. Boroyevich, R. Burgos, P. Mattavelli, and Z. Shen, "Impedance-based analysis of grid-synchronization stability for three-phase paralleled converters," *IEEE Trans. Power Electron.*, vol. 31, no. 1, pp. 26–38, Jan. 2016.

[6] X. Feng, J. Liu, and F. C. Lee, "Impedance specifications for stable DC distributed power systems," *IEEE Trans. Power Electron.*, vol. 17, no. 2, pp. 157–162, Mar. 2002.

[7] P. Xiao, G. K. Venayagamoorthy, and K. A. Corzine, "A novel impedance measurement technique for power electronic systems," in *Proc. IEEE Power Electron. Specialists Conf.*, Jun. 2007, pp. 955–960.

[8] A. G. J. MacFarlane and I. Postlethwaite, "The generalized Nyquist stability criterion and multivariable root loci," *Int. J. Control*, vol. 25, no. 1, pp. 81–127, 1977.

[9] J. Jokipii, T. Messo, and T. Suntio, "Simple method for measuring output impedance of a three-phase inverter in *dq*-domain," in *Proc. IEEE Power Electron. Conf.*, May. 2014, pp. 1466–1470.

[10] A. Riccobono, M. Mirz, and A. Monti, "Noninvasive online parametric identification of three-phase AC power impedances to assess the stability of grid-tied power electronic inverters in LV networks," *IEEE J. Emerg. Sel. Topics Power Electron.*, vol. 6, no. 2, pp. 629–647, Jun. 2018.

[11] Z. Shen, "Online measurement of three-phase AC power system impedance in synchronous coordinates," Ph.D. Dissertation, Dept. Elect. Eng., Virginia Tech, Blacksburg, VA, USA, 2012.

[12] G. Francis, R. Burgos, D. Boroyevich, F. Wang, and K. Karimi, "An algorithm and implementation system for measuring impedance in the D-Q domain," in *Proc. Energy Convers. Congr. Expo.*, Sep. 2011, pp. 32–28.

[13] J. Huang, K. A. Corzine, and M. Belkhayat, "Small-signal impedance measurement of power-electronics-based AC power systems using line-to-line current injection," *IEEE Trans. Power Electron.*, vol. 24, no. 2, pp. 445–455, Feb. 2009.

[14] I. Cvetkovic, M. Jaksic, D. Boroyevic, P. Mattavelli, and F. C. Lee, "Un-terminated, low-frequency terminal-behavioral d-q model of three-phase converters," in *Proc. Energy Convers. Congr. Expo.*, Sep. 2011, pp. 791–798.

[15] I. Cvetkovic, D. Boroyevich, P. Mattavelli, F. C. Lee, and D. Dong, "Un-terminated, low-frequency terminal behavioral model of dc-dc converters," in *Proc. Appl. Power Electron. Conf. Expo.*, Mar. 2011, pp. 1873–1880.

[16] V. Valdivia, P. Mattavelli, B. Wen, M. Jaksic, A. Lazaro, and A. Barrado, "Confidence analysis on identification results of three-phase voltage source inverters *d-q* impedance from transient response to load steps," in *Proc. Appl. Power Electron. Conf. Expo.*, Mar. 2013, pp. 2726–2733.

[17] T. Roinila, J. Huusari, and M. Vilkko, "On frequency-response measurements of power-electronic systems applying MIMO identification techniques," *IEEE Trans. Ind. Electron.*, vol. 60, no. 11, pp. 5270–5276, Nov. 2013.

[18] R. Luhtala, T. Roinila, and T. Messo, "Implementation of real-time impedance-based stability assessment of grid-connected systems using MIMO-identification techniques," *IEEE Trans. Ind. Appl.*, vol. 54, no. 5, pp. 5054–5063, Sep. 2018.

[19] T. Roinila, T. Messo, and E. Santi, "MIMO-identification techniques for rapid impedance-based stability assessment of three-phase systems in DQ domain," *IEEE Trans. Power Electron.*, vol. 33, no. 5, pp. 4015–4022, May 2018.

[20] T. Roinila, T. Messo, and A. Aapro, "Impedance measurement of three phase systems in DQ-domain: Applying MIMO-identification techniques," in *Proc. Energy Convers. Congr. Expo.*, Sep. 2016, pp. 1–6.

[21] B. Wen, D. Boroyevich, R. Burgos, P. Mattavelli, and Z. Shen, "Small-signal stability analysis of three-phase AC systems in the presence of constant power loads based on measured *d-q* frame impedances," *IEEE Trans. Power Electron.*, vol. 30, no. 10, pp. 5952–5963, Oct. 2015.

[22] Z. Yao, P. G. Therond, and B. Davat, "Stability analysis of power systems by the generalised Nyquist criterion," in *Proc. Int. Conf. Control*, Mar. 1994, pp. 739—-744.

[23] Y. A. Familiant, J. Huang, K. A. Corzine, and M. Belkhayat, "New techniques for measuring impedance characteristics of three-phase AC power systems," *IEEE Trans. Power Electron.*,vol. 24, no. 7, pp. 1802–1810, Jul. 2009.

[24] B. Zhou and M. Jacsic, "Small-signal impedance identification of three-phase diode rectifier with multi-frequency injection," in *Proc. Appl. Power Electron. Conf. Expo.*, Mar. 2014, pp. 2746–2753.

[25] V. Valdivia, A. Lazaro, A. Barrado, P. Zumel, C. Fernandez, and M. Sanz, "Black-box modeling of three-phase voltage source inverters for system-level analysis," *IEEE Trans. Ind. Electron.*, vol. 59, no. 9, pp. 3648–3662, Sep. 2012.

[26] V. Valdivia, A. Lázaro, A. Barrado, P. Zumel, C. Fernández, and M. Sanz, "Impedance identification procedure of three-phase balanced voltage source inverters based on transient response measurements," *IEEE Trans. Power Electron.*, vol. 26, no. 12, pp. 3810–3816, Dec. 2011.

[27] L. Ljung, I. Gustavsson, and T. Soderstrom, "Identification of linear, multivariable systems operating under linear feedback control," *IEEE Trans. Autom. Control*, vol. 19, no. 6, pp. 836–840, Dec. 1974.

[28] L. Ljung, *System Identification: Theory for the User.* 2nd ed. Englewood Cliffs, NJ, USA: Prentice-Hall, 1999.

[29] A. Bazanella, M. Gevers, and L. Miškovic, "Closed-loop identification of MIMO systems: A new look at identifiability and experiment design," *Eur. J. Control*, vol. 16, no. 3, pp. 228–239, 2010.

[30] H. Gong, D. Yang, and X. Wang, "Impact analysis and mitigation of synchronization dynamics for DQ impedance measurement," *IEEE Trans. Power Electron.*, vol. 34, no. 9, pp. 8797–8807, Sep. 2019.

Hong Gong (Student Member, IEEE) was born in Sichuan, China, in 1992. He received the B.S and M.S. degrees from Sichuan University, Chengdu, China, in 2014 and 2017, respectively. He is currently working toward the Ph. D. degree with the Aalborg University, Aalborg, Denmark.

His research interests include modeling and control of grid-connected converters, and impedance measurement.

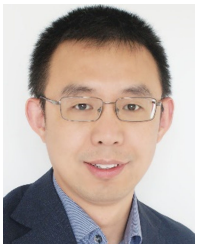

Xiongfei Wang (Senior Member, IEEE) received the B.S. degree from Yanshan University, Qinhuangdao, China, in 2006, the M.S. degree from the Harbin Institute of Technology, Harbin, China, in 2008, both in electrical engineering, and the Ph.D. degree in energy technology from Aalborg University, Aalborg, Denmark, in 2013.

Since 2009, he has been with the Department of Energy Technology, Aalborg University, where he became an Assistant Professor in 2014, an Associate Professor in 2016, a Professor and a Research Program Leader for Electronic Power Grid (eGrid) in 2018, and the Director of Aalborg University-Huawei Energy Innovation Center in 2020. He is also a part-time Visiting Professor of power electronics systems with KTH Royal Institute of Technology, Stockholm, Sweden. His current research interests include modeling and control of grid-interactive power converters, stability and power quality of power-electronic-based power systems, active and passive filters.

Dr. Wang was selected into Aalborg University Strategic Talent Management Program in 2016. He was the recipient of received six IEEE Prize Paper Awards, the 2016 Outstanding Reviewer Award of IEEE TRANSACTIONS ON POWER ELECTRONICS, the 2018 IEEE PELS Richard M. Bass Outstanding Young Power Electronics Engineer Award, the 2019 IEEE PELS Sustainable Energy Systems Technical Achievement Award, and the 2019 Highly Cited Researcher by Clarivate Analytics (former Thomson Reuters). He serves as a Member-at-Large for Administrative Committee of IEEE Power Electronics Society from 2020 to 2022, and as an Associate Editor for the IEEE TRANSACTIONS ON POWER ELECTRONICS, the IEEE TRANSACTIONS ON INDUSTRY APPLICATIONS, and the IEEE JOURNAL OF EMERGING AND SELECTED TOPICS IN POWER ELECTRONICS.

Dongsheng Yang (Senior Member, IEEE) received the B.S., M.S., and Ph.D. degrees in electrical engineering from the Nanjing University of Aeronautics and Astronautics, Nanjing, China, in 2008, 2011, and 2016, respectively.

In 2016, he was a Postdoc Researcher with Aalborg University, Aalborg, Denmark, where he became an Assistant Professor with the Department of Energy Technology in 2018. Since 2019, he has been an Assistant Professor within the Electrical Energy Systems group, Eindhoven University of Technology, Eindhoven, The Netherlands. His main research interests include modeling, analysis, and control of grid-interactive converters, harmonic and resonance mitigation of large-scale power electronics-based power system, impedance measurement technique for real-field harmonic instability assessment, and innovative hardware of power-electronics-based infrastructure for future power grids.